Journal of Catalysis 258 (2008) 393–400

Contents lists available at ScienceDirect

Journal of Catalysis

www.elsevier.com/locate/jcat

The active site of nickel phosphide catalysts for the hydrodesulfurization of 4,6-DMDBT

S. Ted Oyama [a,*], Yong-Kul Lee [b]

[a] Environmental Catalysis and Nanomaterials Laboratory, Department of Chemical Engineering (0211), Virginia Tech, Blacksburg, VA, 24061, USA
[b] Department of Chemical Engineering, Dankook University, 126 Jukjeondong, Yongin 448-701, South Korea

ARTICLE INFO

Article history:
Received 24 April 2008
Revised 11 June 2008
Accepted 16 June 2008

Keywords:
Nickel phosphide
XRD
EXAFS
4,6-Dimethyldibenzothiophene
Hydrodesulfurization
Active site
Direct desulfurization pathway
Hydrogenation pathway

ABSTRACT

Ni_2P catalysts supported on SiO_2 and MCM-41 were prepared by temperature-programmed reduction (TPR), and the effect of the dispersion on catalyst structure and hydroprocessing performance was studied. The surface areas of the samples varied from low (Ni_2P/SiO_2-L, 88 $m^2\,g^{-1}$) to high (Ni_2P/SiO_2-H, 240 $m^2\,g^{-1}$), to very high (Ni_2P/MCM-41, 487 $m^2\,g^{-1}$), with corresponding Ni_2P average crystallite sizes decreasing from 10.1 to 6.5 and 3.8 nm. X-ray diffraction (XRD) and extended X-ray absorption fine structure (EXAFS) studies were used to obtain structural parameters for the supported Ni_2P phase. The catalytic activity in hydrodesulfurization (HDS) was measured at 613 K and 3.1 MPa in a three-phase fixed bed reactor using a model liquid feed containing 4,6-dimethyldibenzothiophene (4,6-DMDBT) and quinoline in a tridecane solvent. At standard conditions using 500 ppm S as 4,6-DMDBT, 6000 ppm S as dimethyldisulfide (DMDS), and 500 ppm N as quinoline, the catalytic activity followed the sequence Ni_2P/MCM-41 > Ni_2P/SiO_2-H > Ni_2P/SiO_2-L, based on equal sites (230 μmol) loaded in the reactor. In particular, Ni_2P/MCM-41 gave an HDS conversion of 90%, which was much higher than that of a commercial Ni–Mo–S/Al_2O_3 catalyst which gave an HDS conversion of 68%, based on equal number of sites (230 μmol) loaded in the reactor. The sites were counted by CO chemisorption for the phosphide and by low-temperature O_2 chemisorption for the sulfide. EXAFS analysis of the samples confirmed the presence of two types of sites, tetrahedral Ni(1) sites and square pyramidal Ni(2) sites, with the latter growing in number in the same order as the reactivity Ni_2P/MCM-41 > Ni_2P/SiO_2-H > Ni_2P/SiO_2-L, as the crystallite size decreased. From the selectivity to the direct desulfurization (DDS) product (dimethylbiphenyl) and the hydrogenation (HYD) products (methylcyclohexyltoluenes and dimethylbicyclohexyls) it is concluded that the Ni(1) sites are responsible for DDS while the Ni(2) are highly active sites for the HYD route.

1. Introduction

The removal of sulfur from petroleum feedstocks is important for air quality control. The presence of sulfur oxides in automotive engine exhaust inhibits and poisons noble metal catalysts in catalytic converters, resulting in the emissions of non-combusted hydrocarbons, nitrogen oxides, and carbon monoxide. Such emissions are catalyzed by sunlight to form ground level ozone, and together form smog. In recent years sulfur removal has become a *pressing* problem because of the introduction of strict environmental laws limiting the sulfur content in transportation fuels. For example, in 2006 the US sulfur contents in gasoline were mandated to be 30 ppm (with an 80 ppm cap) in gasoline and 15 ppm in diesel [1], and similar levels had been legislated in Europe and Japan [2–4]. By 2008, the standards effectively require diesel to reach 10 ppm S content and every blend of gasoline sold in the United States to meet the 30 ppm level [5]. Such levels correspond to the removal of +99.99% of sulfur from a typical crude containing 1.5% sulfur, and the removal process has been termed deep or ultra-deep HDS.

Among alternatives to the widely used sulfides are transition metal carbides, nitrides, and phosphides [6–11]. Metal phosphides are a novel catalyst group for deep hydrotreating and have received much attention due to their high activity for hydrodesulfurization (HDS) and hydrodenitrogenation (HDN) of petroleum feedstocks [18–21]. Transition metal phosphide catalysts have been studied in hydrogenation reactions [22–25] but research focusing on hydrotreating has been carried out only relatively recently [9–17,26–32]. These studies have been enhanced by theoretical treatments [33,34].

It has been found that transition metal phosphides can be easily synthesized by temperature programmed reduction (TPR) of oxidic precursors (metal phosphates) at moderately high temperatures (773–873 K) [5]. Among the phosphides studied, the group 6 and iron group compounds have shown good activity in hy-

* Corresponding author.
E-mail address: oyama@vt.edu (S.T. Oyama).

0021-9517/$ – see front matter
doi:10.1016/j.jcat.2008.06.023

droprocessing [10,35,38]. In a previous study at 643 K and 3.1 MPa, the overall activity was found to follow in the order: Fe_2P/SiO_2 < CoP/SiO_2 < MoP < WP < Ni_2P/SiO_2 in the HDS of dibenzothiophene (3000 ppm S) and in the HDN of quinoline (2000 ppm N), in which the comparison was made based on equal sites (230 μmol CO/O_2 for phosphides/sulfides) loaded in the reactor [35,36]. Among the group 6 compounds, bulk MoP and WP were more active for the HDN of quinoline than sulfides. It has been shown that MoP could be well dispersed on a SiO_2 support (Cab-O-Sil, M5, 200 $m^2\,g^{-1}$) and that it had four times higher activity in the HDS of thiophene than MoS_2/SiO_2 [37], at 643 K under atmospheric pressure. The effect of phosphorus content has been studied in Ni_2P catalysts [38,39]. For Ni_2P/SiO_2 catalysts [38] with varying atomic ratio of Ni to P in the oxidic precursors, excess P (initial Ni/P ratio = 1/2) gave more dispersed and stable phases with higher activity (dibenzothiophene HDS conversion of 100% and quinoline HDN conversion of 81% at a LHSV of 0.65 h^{-1}). A study of the electronic properties of SiO_2 supported Ni_2P, MoP, and MoS_2 catalysts has been made using density functional calculations [40]. In this study it was found that the electron density around the metal followed the order, MoS_2/SiO_2 < MoP/SiO_2 < Ni_2P/SiO_2, which correlated well with the thiophene HDS activities of the catalysts. It was suggested that electron transfer from the metal cation to the non-metal could enhance HDS activity by facilitating the dissociation of H_2 and the adsorption of thiophene [40,41]. The results above suggest that Ni_2P catalysts are promising in the deep HDS area where considerable improvements in activity are required to obtain conversions above 99.99%.

Previous studies of silica-supported Ni_2P employed a low surface area (90 $m^2\,g^{-1}$) support (SiO_2-L) [38,42,43]. It is the objective of this work to investigate a high surface area silica (350 $m^2\,g^{-1}$) (SiO_2-H) and a mesoporous siliceous material (790 $m^2\,g^{-1}$) (MCM-41) as supports. As will be shown, the samples prepared on the higher surface area materials have Ni_2P in smaller crystallite size, and EXAFS analysis shows that these smaller crystallites have proportionately higher quantities of five-fold coordinated square-pyramidal Ni sites than four-fold coordinated tetrahedral Ni sites. The presence of these sites correlates with the catalytic activity, indicating that they are the active sites for the HDS reaction.

2. Experimental

2.1. Synthesis of supported Ni_2P catalysts

Commercial SiO_2 supports (Cabot, Cab-O-Sil) of low surface area (L-90, 90 $m^2\,g^{-1}$) and high surface area (EH-5, 350 $m^2\,g^{-1}$) were used as received. A mesoporous MCM-41 silica support was synthesized following a literature procedure [44]. The chemicals used in the synthesis were colloidal silica (HS-40, Fluka), cetyltrimethylammonium bromide (CTMABr, 99%, Aldrich) and tetramethylammonium hydroxide (TMAOH, 25 wt% aqueous solution, Aldrich). The TMAOH and CTMABr were added to deionized water with stirring at 300 K until the solution became transparent, then the colloidal silica was added to the solution with stirring for 1 h and the resulting reaction gel was aged for 24 h at 323 K. The molar composition was 1.0 SiO_2:0.19 TMAOH:0.27 CTMABr:40 H_2O. After aging, the mixture was reacted for 48 h at 393 K in a Teflon-lined stainless steel autoclave. The product was filtered, washed with distilled water, dried in air at 393 K, and finally calcined at 623 K for 8 h.

The supported Ni_2P catalysts were prepared with excess phosphorus (Ni/P = 1/2) and a loading of 1.16 mmol Ni/g support (12.2 wt% Ni_2P/SiO_2). Previous studies [38,43] had shown that this composition and loading level gave high activity and stability in hydroprocessing reactions. Samples prepared with low surface area silica (L90) were denoted as Ni_2P/SiO_2-L and samples prepared with the high surface area silica (EH5) were denoted as Ni_2P/SiO_2-H. The synthesis of the catalyst involved two steps and was described elsewhere [38]. Briefly, in the first step, a supported nickel phosphate precursor was prepared by incipient wetness impregnation of a solution of nickel nitrate and ammonium phosphate, followed by calcination at 673 K. In the second step, the supported metal phosphate was reduced to a phosphide by temperature-programmed reduction (TPR). In the TPR procedure, which was also used to determine the reduction characteristics of the material, 0.20 g of material was loaded in a quartz glass u-tube reactor and the effluent was monitored by a mass spectrometer (Ametek/Dycor MA100). In catalyst preparation, larger batches using up to 5.50 g of supported nickel phosphate were prepared in a similar manner by reduction to 873, 883, and 893 K for Ni_2P/SiO_2-L, Ni_2P/SiO_2-H, and Ni_2P/MCM-41, respectively. The final reduction temperatures were determined by TPR traces to be presented in Section 3 (Fig. 1). The hydrogen flow rate was set at 1000 μmol s^{-1} (1500 cm^3 (NTP) min^{-1}) per g of sample. At the end of the temperature program the sample was cooled to room temperature in helium and was passivated under 0.5% O_2/He for 6 h.

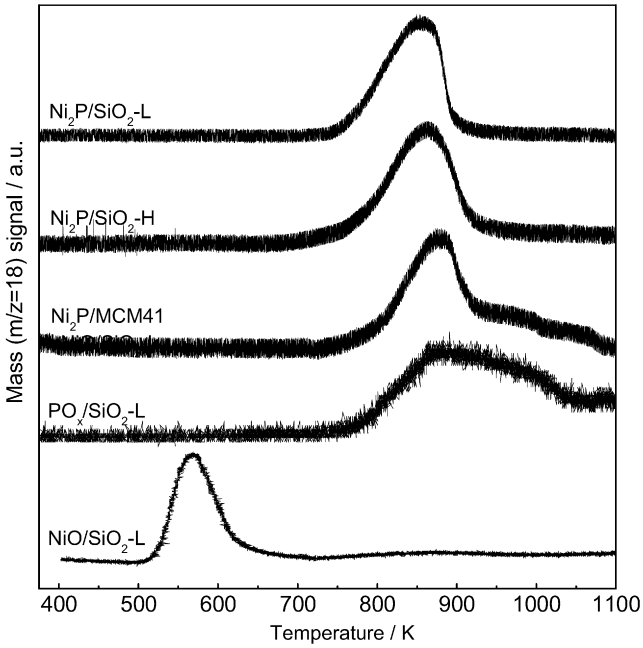

Fig. 1. TPR profiles of supported Ni_2P catalysts.

2.2. Characterization of samples

X-ray diffraction (XRD) patterns of both the freshly prepared and spent samples were obtained with a Scintag XDS-2000 powder diffractometer operated at 45 kV and 40 mA using CuK_α monochromatized radiation ($\lambda = 0.154178$ nm). The average crystallite sizes (D_c) calculated from the Scherrer equation ($D_c = K\lambda/\beta\cos\theta$) [45], where K is a constant taken as 0.9, λ is the wavelength of the X-ray radiation, β is the width of the peak at half-maximum, corrected for instrumental broadening (0.1°), and 2θ is the Bragg angle. Uptakes of CO at room temperature for the phosphides and O_2 at dry-ice/acetone temperature for the sulfide were measured by pulse chemisorption. The use of CO is standard for phosphides and low-temperature, pulse oxygen adsorption is used for sulfides to avoid corrosive chemisorption [11,14,30,36,43]. A Micromeritics ASAP 2010 micropore size analyzer was used to measure the N_2 adsorption/desorption isotherms at 77 K in the samples. Before the measurements, the passivated samples were degassed at 403 K for 12 h. The calculation of the pore size dis-

tribution (PSD) was performed using the Barrett–Joyner–Halenda (BJH) formula [46]. The specific surface area of the sample was calculated from the linear portion of BET plots ($P/P_0 = 0.01$–0.10), and the cumulative surface area of the mesopores was obtained from PSD curves. The chemical composition of the samples was determined by inductively coupled plasma-absorption emission spectroscopy (ICP-AES) (Spectro Analytical Instruments, Model Spectroflame FTMO A85D). For complete dissolution of the samples, aqua regia digestion was carried out with heating in a microwave oven (EthosPlus, Milestone).

X-ray absorption (XAS) spectra at the Ni K edge (8.333 keV) of reference and catalyst samples were recorded in the energy range 8.233 to 9.283 keV using synchrotron radiation at the National Synchrotron Light Source (NSLS) at Brookhaven National Laboratory (BNL), beamline X18B. The X-ray ring at the NSLS has a flux of 1×10^{10} photons s^{-1} at 100 mA and 2.5 GeV. The monochromator is equipped with a Si (111) channel-cut single crystal and has an energy range capability of 5.8 to 40 keV. The crystal was detuned slightly to prevent glitches due to harmonics. Extended X-ray absorption fine structure spectra (EXAFS) were recorded at ambient temperature in transmission mode using ionization chambers for the detection of primary (I_0, 100% N_2) and transmitted (I_t, 75% N_2, balance Ar) beam intensities. Bulk reference samples were diluted with BN (0.1 g catalyst + 0.3 g BN). The samples were reduced in reactors at the same conditions as before reaction and were transferred to glass cells with Kapton windows without exposure to the atmosphere. The obtained EXAFS data were analyzed by Winxafs 97. In order to fit the experimental EXAFS spectra for the fresh and spent samples, the theoretical EXAFS equation for Ni_2P was used to calculate phase shifts and amplitude functions of Ni_2P, using FEFF 8.0 code [47]. Fitting was then carried out for the fresh samples using the three dominant shells (2 Ni–P at 0.2266 nm, 4 Ni–P at 0.2457 and 4 Ni–Ni at 0.2678 nm), using a reducing factor (S_0^2), fixed as 0.90, a value obtained by fitting the Ni–Ni contribution in Ni foil.

2.3. Activity test for HDS

Hydrotreating was carried out at 3.1 MPa (450 psig) and 613 K (340 °C) in a three-phase upflow fixed-bed reactor using a model feed mixture containing sulfur, nitrogen, aromatic and aliphatic compounds. The feed liquid was prepared by combining 500 ppm (0.05 wt%) sulfur as 4,6-dimethyldibenzothiophene (4,6-DMDBT, Fisher, 95%), 6000 ppm (0.6 wt%) sulfur as dimethyldisulfide (DMDS, Aldrich, 99%), 500 ppm (0.05 wt%) nitrogen as quinoline (Aldrich, 99%), 1% aromatics as tetralin (Aldrich, 99%), with *n*-tridecane (Alfa Aesar, 99%) as solvent, and *n*-octane (Aldrich, 99%) as an internal reference. The liquid was delivered at 0.0833 $cm^3\,s^{-1}$ (5 $cm^3\,h^{-1}$) using a liquid pump along with 100 μmol s^{-1} (150 cm^3 (NTP) min^{-1}) hydrogen flow. Liquid product compositions were determined with a Hewlett Packard 5890A gas chromatograph, equipped with a 50 m dimethylsiloxane column having 0.32 mm i.d. (Chrompack, CPSil 5B), on samples collected at 4- to 5-h intervals. Reaction products were identified by matching retention times with commercially available standards, as well as by GC/MS analysis. The GC/MS combined a Fisons Carlo Erba 8060 series gas chromatograph, using a HP-5MS 5% phenylmethylsiloxane stationary phase, with a VG Quattro triple quadrupole mass spectrometer operated in the electron impact-positive ion mode. Quantities of catalysts loaded in the reactor corresponded to the same amount of CO or atomic oxygen uptake (230 μmol), and were 2.80 g for the Ni_2P/SiO_2-L catalyst, 2.3 g for the Ni_2P/SiO_2-H catalyst, 1.70 g for the Ni_2P/MCM-41 catalyst and 0.83 g for the Ni–Mo–S/Al_2O_3 catalyst, with corresponding liquid hourly space velocity (LHSV) of 0.65, 0.80, 1.10, and 4.0 h^{-1}. For the hydroprocessing reaction the passivated phosphide catalysts were pretreated for 2 h at 723 K in 100 μmol s^{-1} (150 cm^3 (NTP) min^{-1}) of H_2, and the sulfide catalyst was pretreated at 578 K for 2 h with 100 μmol s^{-1} of 10% H_2S/H_2 at a pressure slightly above 1 atm. The reaction system was allowed to run for 40–50 h to establish steady-state. The results of several measurements were averaged. The 4,6-dimethyldibenzothiophene (4,6-DMDBT) molecule undergoes HDS via two parallel reaction pathways: (i) direct desulfurization (DDS) leading to the formation of 3,3-dimethylbiphenyl (3,3-DMBP) and (ii) prehydrogenation followed by desulfurization (HYD) giving first 4,6-tetrahydro- and hexahydrodibenzothiophenes, which are further desulfurized to methylcyclohexyltoluenes (MCHT) and dimethylbicyclohexyls (DMBCH).

Table 1
Physical properties of supported Ni_2P samples

Sample	Condition	CO uptake (μmol g^{-1})	N_2 adsorption	
			BET area ($m^2\,g^{-1}$)	Pore volume ($cm^3\,g^{-1}$)
SiO_2-L	–	–	92	–
Ni_2P/SiO_2-L	Fresh	85	88	–
SiO_2-H	–	–	350	–
Ni_2P/SiO_2-H	Fresh	112	240	–
MCM-41, calcined	–	–	789	0.71
Ni_2P/MCM-41	Fresh	139	487	0.41

In this paper, the HDS conversion and the selectivities are defined as

$$\text{HDS conversion (\%)} = 100 \times \left(1 - \frac{\text{MCHT} + \text{DMBCH} + \text{3,3DMBP}}{\text{4,6DMDBT}_{\text{in}}}\right),$$

$$\text{HYD selectivity (\%)} = 100 \times \left(\frac{\text{MCHT} + \text{DMBCH}}{\text{4,6DMDBT}_{\text{in}} - \text{4,6DMDBT}_{\text{out}}}\right),$$

$$\text{DDS selectivity (\%)} = 100 \times \left(\frac{\text{3,3DMBP}}{\text{4,6DMDBT}_{\text{in}} - \text{4,6DMDBT}_{\text{out}}}\right).$$

The selectivities are approximate as there is interconversion between dimethylbiphenyl and the cyclohexylbenzene through hydrogenation and dehydrogenation reactions. However, these reactions are relatively slow, and the compounds are not equilibrated.

3. Results

3.1. Structural characterization of supported Ni_2P catalysts

Fig. 1 shows the TPR profiles of the calcined phosphate precursors of the Ni_2P/SiO_2-L, Ni_2P/SiO_2-H, and Ni_2P/MCM-41. The TPR profiles for NiO/SiO_2-L and P_2O_5/SiO_2-L are also shown as references. For the supported Ni_2P/SiO_2-L catalyst a distinct reduction peak at around 850 K is observed with the peak maximum shifting to higher temperature with increase of the surface area of the support. The NiO/SiO_2-L is reduced at a low temperature of around 570 K, while P_2O_5/SiO_2-L over a broad temperature range of 800–1050 K.

Fig. 2 shows the powder XRD patterns of the freshly prepared and passivated Ni_2P samples supported on the low and high surface area silica and the MCM-41 supports, and of a bulk Ni_2P reference material. The XRD patterns confirm that Ni_2P is formed on all supports, with the signals being more broadened for the higher surface area supports. The XRD pattern of the Ni_2P/MCM-41 sample displays the characteristic peaks of the MCM-41 support, with diffraction lines from the (100), (110) and (200) planes of the hexagonal phase [44].

Table 1 summarizes the physical properties of the supported Ni_2P catalyst samples. For the freshly prepared samples, the

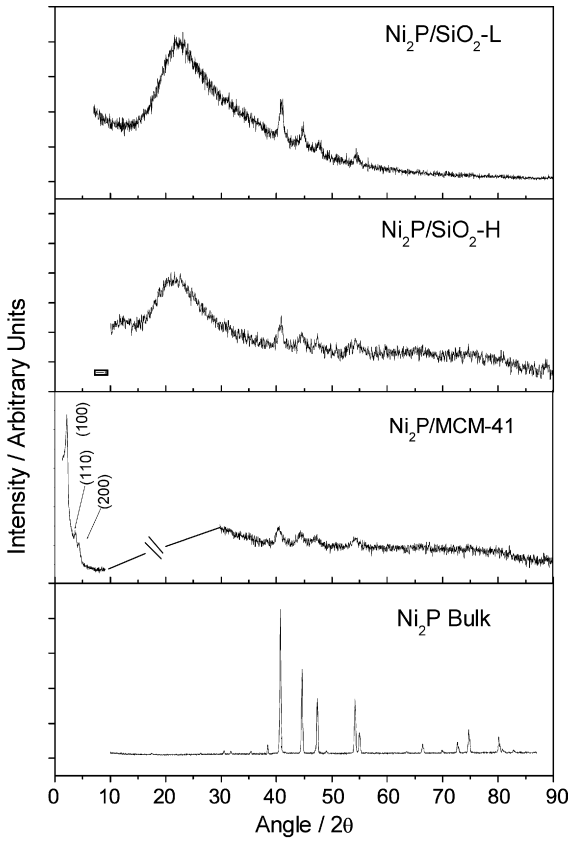

Fig. 2. XRD profiles of supported Ni_2P catalysts.

Table 2
Elemental composition of samples

Sample	Condition	P/Ni molar ratio
Ni_2P (bulk)		0.49
Ni_2P/SiO_2-L	Fresh	0.760
Ni_2P/SiO_2-H	Fresh	0.963
Ni_2P/MCM-41	Fresh	1.113

amount of CO uptake increases with the surface area of the support. The BET surface area and pore volume for the Ni_2P/MCM-41 were much lower than those of the calcined MCM-41.

Table 2 gives the nickel, phosphorous, and sulfur concentrations of the samples before reaction as determined by ICP-AES. All of the samples were prepared with an initial Ni/P ratio of 1/2. In all cases the freshly prepared samples were found to have phosphorus contents that were smaller than the initial value, with Ni/P ratios ranging from 1/0.76 to 1/1.113. More P remained for the samples with higher dispersion.

Fig. 3 shows the Ni K-edge EXAFS spectra, Fourier transforms and Fourier filtered EXAFS spectra of the freshly prepared samples and a bulk reference Ni_2P sample. For the bulk Ni_2P, the Fourier transform gives two main peaks, a smaller peak at 0.171 nm, and a larger peak at 0.228 nm. For the supported Ni_2P samples there are also two main peaks located at almost the same positions as those of the bulk Ni_2P reference, but with the larger peak weakened and broadened as the surface area of the support increases, and the smaller peak growing in prominence.

Table 3 summarizes the curve-fitting results of the EXAFS spectra for the freshly prepared Ni_2P samples, the reference experimental bulk Ni_2P sample and crystallographic Ni_2P standard data from the literature [47]. For the bulk Ni_2P the coordination numbers of the first (Ni(1)–P) and third (Ni–Ni) shell are in good agreement with those of the standard Ni_2P with the bond lengths being slightly lowered, while the coordination number of the second shell (Ni(2)–P) is much lower than that of reference Ni_2P (1.75 vs 4.0). For the supported Ni_2P samples in the first shell the Ni(1)–P coordination number remains constant at around 2.0, with the bond distance being lowered. In the second shell the Ni(2)–P coordination number increases with increase of catalyst dispersion, while the bond distance decreases. In the third shell the Ni–Ni coordination number decreases with catalyst dispersion (3.43, 3.05, and 2.88 for Ni_2P/SiO_2-L, Ni_2P/SiO_2-H, and Ni_2P/MCM-41, respectively), while the bond distance increases slightly.

3.2. Activity test for HDS of 4,6-DMDBT

Fig. 4 shows the HDS conversion and product selectivities for the Ni_2P/SiO_2-L and Ni_2P/SiO_2-H samples in the DDS and HYD pathways of 4,6-DMDBT as a function of time on stream at 613 K (340 °C). The conversion was 62% for Ni_2P/SiO_2-L and 82% for Ni_2P/SiO_2-H. The selectivity for the HYD pathway was 34% for Ni_2P/SiO_2-L and 50% for Ni_2P/SiO_2-H.

Fig. 5 shows the HDS conversion of 4,6-DMDBT and the product selectivities toward DDS and HYD for the Ni_2P/MCM-41 and Ni–Mo–S/Al_2O_3 catalyst as a function of time on stream at 613 K (340 °C). The conversion was 90% for Ni_2P/MCM-41 and 68% for Ni–Mo–S/Al_2O_3. The selectivity to HYD was 65% for Ni_2P/MCM-41 and 73% for Ni–Mo–S/Al_2O_3.

4. Discussion

4.1. The nature of the supported Ni_2P catalysts

Ni_2P [47,48] adopts a hexagonal structure (Space group: $P_{\bar{6}2m}$, D^2_{3h}, Struckturbericht notation: revised C22) with lattice parameters, $a = b = 0.5859$ nm, $c = 0.3382$ nm, in which the Ni atoms form two types of 9-fold arrangements around each P atom. Both 9-fold arrangements consist of a Ni trigonal prism around a P and three additional Ni atoms bonded to the center P through the three rectangular faces of the trigonal prism. There are two types of Ni (denoted as Ni(1), Ni(2)) and P (denoted as P(1), P(2)) sites, which form two different trigonal prisms in Ni_2P (Fig. 6). For example, the Ni(1) site is quasi tetrahedral surrounded by 4 nearest-neighbor P atoms (2 P(2) at 0.2209 nm and 2 P(1) at 0.2266 nm) and 8 second-nearest neighbor Ni atoms (2 Ni(1) at 0.2613 nm, 2 Ni(2) at 0.2605 nm, and 4 Ni(2) at 0.26783 nm). The Ni(2) site is square pyramidal surrounded by 5 nearest-neighbor P atoms (1 apical P(1) at 0.2369 nm, 4 basal P(2) at 0.2456 nm) and 6 next-nearest-neighbor Ni atoms (2 Ni(1) at 0.2605 nm, and 4 Ni(1) at 0.26783 nm). As will be discussed, the Ni(1) site is likely involved in the direct desulfurization pathway in HDS while Ni(2) site is responsible for the high catalytic activity in the hydrogenation pathway in HDS.

Ni_2P catalysts were successfully prepared on the SiO_2 and MCM-41 supports. The temperature programmed reduction profile for the calcined nickel phosphate precursors gives a distinctive reduction peak at a moderately high temperature of around 873 K (Fig. 1). In the case of PO_x/SiO_2 a broad reduction feature is observed at high temperature, indicating that the phosphate is difficult to reduce. In the case of NiO/SiO_2 the reduction occurs at a lower temperature, 570 K, consistent with the known reducibility of nickel oxide [49]. These results indicate that Ni species in the oxidic precursor are strongly associated with the P component. Furthermore, the peak maximum of reduction temperature is shifted to slightly higher temperature for the samples with better dispersion, and this implies that smaller crystallites have stronger interaction between the Ni and the phosphorus.

The samples were prepared with excess phosphorus using a P/Ni ratio of 2/1. Elemental analysis shows that there was a loss

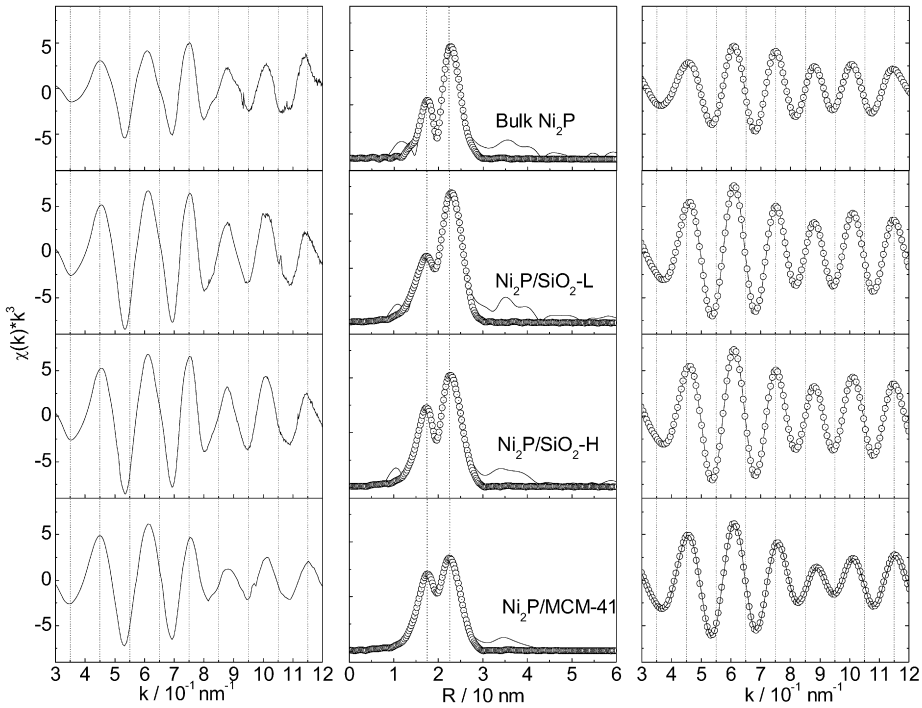

Fig. 3. EXAFS analysis results: Ni K-edge EXAFS spectra (left), Fourier transforms (middle) and Fourier filtered EXAFS spectra (right). The solid lines are the experimental curves and the circles are calculated points.

Table 3
Curve-fitting results for Ni_2P catalysts

Samples	Ni–P								Ni–Ni(1, 2)				R (%)
	Ni–P(1) (tetrahedral Ni)				Ni–P(2) (square pyramidal Ni)								
	CN	R (nm)	σ^2 (10^{-5} nm^2)	ΔE (eV)	CN	R (nm)	σ^2 (10^{-5} nm^2)	ΔE (eV)	CN	R (nm)	σ^2 (10^{-5} nm^2)	ΔE (eV)	
Ni_2P FEFF	2	0.2209			1	0.2369			4	0.2678			
Reference	2	0.2266			4	0.2457							
Ni_2P (bulk)	2.0	0.2253	3.00	0.420	1.750	0.2401	0.499	0.423	3.99	0.2644	6.00	1.798	0.48
Ni_2P/SiO_2-L	1.99	0.2234	4.900	−2.397	2.57	0.2399	6.352	−2.392	3.43	0.2612	8.001	−0.389	0.962
Ni_2P/SiO_2-H	1.98	0.2225	6.420	−4.260	3.191	0.2383	8.460	−4.261	3.05	0.2625	8.159	−1.156	1.048
Ni_2P/MCM-41	1.99	0.2210	2.884	−0.448	3.482	0.2375	4.361	−0.381	2.88	0.2631	8.477	−2.290	1.249

ΔR filtered = 0.1427–0.27598 nm, $S_0^2 = 0.9$. Residual $(R, \%) = \left(\frac{\sum_{i=1}^{N} |y_{\exp}(i) - y_{\text{theo}}(i)|}{\sum_{i=1}^{N} y_{\exp}(i)}\right) \times 100$.

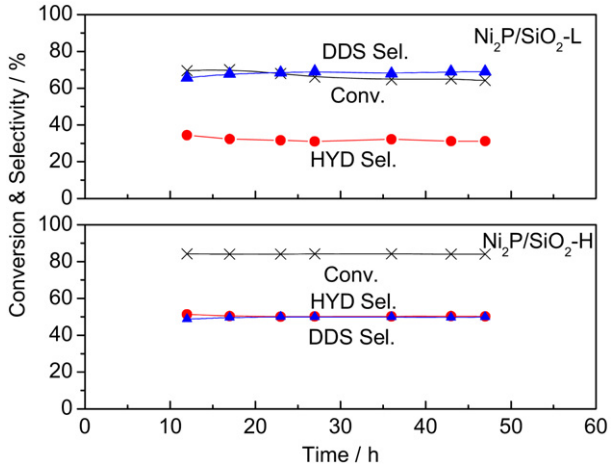

Fig. 4. Activity test in HDS of 4,6-DMDBT for SiO_2 supported Ni_2P catalysts at 340 °C. Sulfur as 4,6-DMDBT 0.05%, sulfur as DMDS 0.6%, tetralin 1%, nitrogen as quinoline 0.05%.

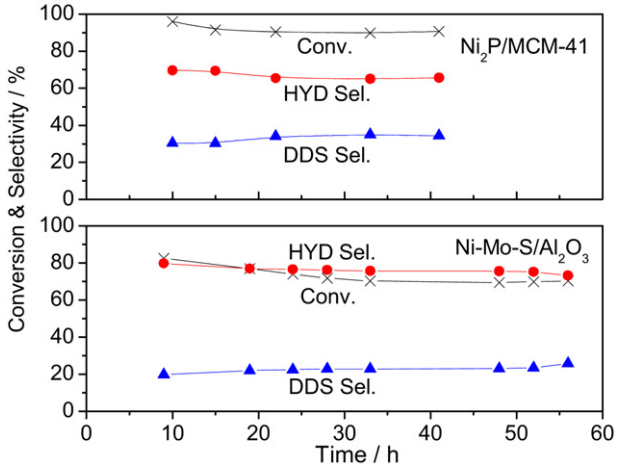

Fig. 5. Activity test in HDS of 4,6-DMDBT for Ni_2P/MCM-41 and Ni–Mo–S/Al_2O_3 at 340 °C. Sulfur as 4,6-DMDBT 0.05%, sulfur as DMDS 0.6%, tetralin 1%, nitrogen as quinoline 0.05%.

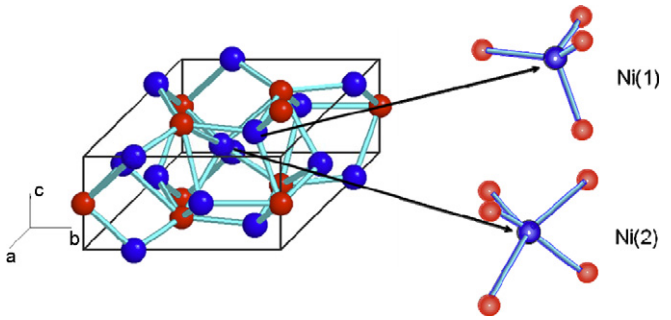

Fig. 6. Ni(1) and Ni(2) sites in Ni_2P.

of the phosphorus during preparation (Table 2) with P/Ni ratios of 0.76–1.1, approaching the stoichiometric value of 0.5 for Ni_2P. Previous work had shown that phosphorus is removed as PH_3 during the reduction procedure and that some P was left on the support [36,42]. Elemental analysis revealed that more P remained on the better dispersed supported Ni_2P catalysts (Table 2), even though higher temperatures were applied for reducing these well dispersed samples (873, 883, and 893 K for Ni_2P/SiO_2-L, Ni_2P/SiO_2-H, and Ni_2P/MCM-41, respectively). This again is consistent with stronger interactions between Ni and P in the smaller crystallites. On all the supports the characteristic XRD signals of Ni_2P are clearly visible (Fig. 2), although the overall peak intensity is progressively lowered for the higher surface area supports. Compared to the Ni_2P/SiO_2-L sample the Ni_2P XRD peaks become increasingly broader and less intense in going to the Ni_2P/SiO_2-H and Ni_2P/MCM-41 materials indicating increasingly dispersed Ni_2P crystallites, as also indicated by the growth in the CO uptake (Table 1). The retention of the MCM-41peaks indicates that the framework structure does not deteriorate seriously during the synthesis steps which include calcination at 673 K followed by reduction at 893 K.

EXAFS analysis is particularly useful for characterizing highly dispersed phases on supports with large surface area. Fourier transform EXAFS spectra for the supported Ni_2P catalysts show two overlapping peaks in the region 0.15–0.30 nm. A simple analysis of the spectra was precluded because it was not possible to extract directly from the experimental spectra the phase shifts and backscattering amplitude functions needed for the fits due to the insufficient separation of the peaks corresponding to the Ni and P neighbors and the possible superposition in the second shell of both the Ni and the P contributions. The spectrum of the reference Ni_2P compound was therefore first simulated with FEFF 8.0 code [50], with structural parameters obtained from the literature [47]. The FEFF simulation (circles in Fig. 5) allowed the assignment of those peaks that appeared in the Fourier transform. The first small peak centered at 0.180 nm was due to P neighbors at 0.2209 and 0.2266 nm and the second larger peak centered at 0.230 nm was due to a mixed feature of P neighbors at 0.2369 and 0.2457 nm and of Ni neighbors at 0.26783 nm. Since the number of independent fitting parameters is limited by 12 as given by the formula [51], $N_{ind} = 2\Delta k \Delta R/\pi + 2$, a three-shell analysis is permissible. For the curve fittings the three dominant shells were selected from a simulation result and used as references for phase shift and amplitude calculations. As described above, two Ni–P shells at 0.2266 and 0.2457 nm and one Ni–Ni shell at 0.2678 nm were employed for the calculations. These give reasonable parameters for all samples (Table 3). For example, fitting for bulk Ni_2P gives for Ni–P(1) 2.0 P neighbors at 0.2253 nm and for Ni–P(2) 1.75 P neighbors at 0.2401 nm and 3.99 Ni–Ni neighbors at 0.2644 nm. Based on the Ni_2P structure, there is a P neighbor at 0.2369 nm which is close to the second shell. The decrease in both coordination number and bond length is reasonable because the EXAFS spectrum is an average over the different bonds. In contrast to bulk Ni_2P, for the supported Ni_2P samples the coordination number of the second shell, Ni–P at 0.2457 nm, increases as dispersion increases, even though the Ni–P bond length decreases. Interestingly, the bond length for the Ni–Ni shell increases with the coordination number as the dispersion increases. It is thus likely that the more dispersed Ni_2P catalyst contains more P atoms, and that the interstitial P atoms lengthen the distance between Ni atoms. This is also consistent with the elemental analysis. The Ni_2P/MCM-41 containing highly dispersed Ni_2P crystallites underwent less loss in P, even after the high temperature reduction. This suggests that the smaller crystallites have a stronger interaction between the Ni and P atoms.

Strictly speaking, the analysis in Table 3 gives information about Ni–P(1) and Ni–P(2) bonds, where the Ni can be Ni(1) or Ni(2), from the crystal structure. However, from the number of nearest neighbors the Ni–P(1) bonds are associated with Ni(1) sites and the Ni–P(2) bonds are associated with Ni(2) sites. Overall, the changes in coordination numbers suggest that the number of Ni(2) sites is increasing as the crystallite size goes down. This is because coordination numbers are a measure of the number of bonds. The higher coordination numbers for the Ni–P(2) bonds present a picture of crystallites that have more of these groups as they become smaller, but as the crystallite maintains the bulk Ni_2P structure, this could only arise if the Ni–P(2) bonds are at the surface. Thus, the bulk is terminated with the square pyramidal sites in small crystallites. The square pyramidal sites by definition (five fold coordination vs tetrahedral) have more P, so the P/Ni ratio increases as crystallite size goes down. These square pyramidal sites also stabilize P better. Thus, small crystallites have Ni(2) sites (Fig. 7a).

4.2. Active sites for HDS

The catalytic activity of the supported samples followed the order Ni_2P/MCM-41 > Ni_2P/SiO_2-H > Ni_2P/SiO_2-L. For a feed containing 500 ppm (0.05%) S as 4,6-DMDBT, 6000 ppm (0.6%) S as DMDS, 500 ppm (0.05%) N as quinoline, 1% tetralin, and balance tridecane, the conversion at steady-state at 340 °C was 90% for Ni_2P/MCM-41, 82% for Ni_2P/SiO_2-H, and 62% for Ni_2P/SiO_2-L (Table 4, Figs. 3, 4). This follows the number of Ni(2) sites, as deduced from the increasing coordination of Ni–P(2) sites (Table 3; Fig. 7a). The conclusion is that the square pyramidal Ni(2) sites are responsible for the high HDS activity, and constitute the principal active sites. In a previous study with silica supported samples, the same trend was noted in activity, namely that the higher surface area materials were more active [52]. The levels of conversion were higher in that previous measurement because the feed contained less sulfur and nitrogen. The feed had 500 ppm S as 4,6-DMDBT, 3000 ppm S as dimethyl disulfide, 200 ppm N as quinoline, 1 wt% tetralin, 0.5 wt% *n*-octane (internal standard), and *n*-tridecane (solvent). In another study extra P (Ni/P = 1/2) in the preparation of Ni_2P on the low surface SiO_2 ($\sim$90 $m^2\,g^{-1}$) support gave rise to a better dispersion and also gave a beneficial effect on the catalytic activity as well as the stability [38]. Use of a high surface area siliceous support (MCM-41) has resulted in even higher dispersion, as evident from the amount of CO uptake (Table 1) and the EXAFS line shape analysis, and better catalytic performance.

It should be noted that the characterization is of samples before reaction, and during reaction the Ni(2) sites could change coordination or composition, as they interact with reactants and products. In fact, from previous analysis of the catalysts during and after reaction, it is likely that they take on at least a sulfur atom. Nevertheless, the role of the Ni(2) sites is to provide at least the initial state for the active sites.

Table 4
Correlation between structural properties and catalytic performance

Samples	Surface area ($m^2\,g^{-1}$)	Average crystallite size (D_c) (nm)	Coordination number (CN)		HDS conv. at 613 K	Sel. HYD	Sel. DDS	TOF (s^{-1})
			Ni–P(1)	Ni–P(2)				
Ni_2P (bulk)	–	–	2.0	1.75	–	–	–	
Ni_2P/SiO_2-L	102	10.1	1.99	2.57	62	34	66	4.7×10^{-4}
Ni_2P/SiO_2-H	333	6.5	1.98	3.19	82	50	50	6.2×10^{-4}
Ni_2P/MCM-41	487	3.8	1.99	3.48	90	65	35	6.8×10^{-4}

CO uptakes: Ni_2P/SiO_2-L 85 μmol g^{-1}, Ni_2P/SiO_2-H 112 μmol g^{-1}, Ni_2P/MCM-41 139 μmol g^{-1}.

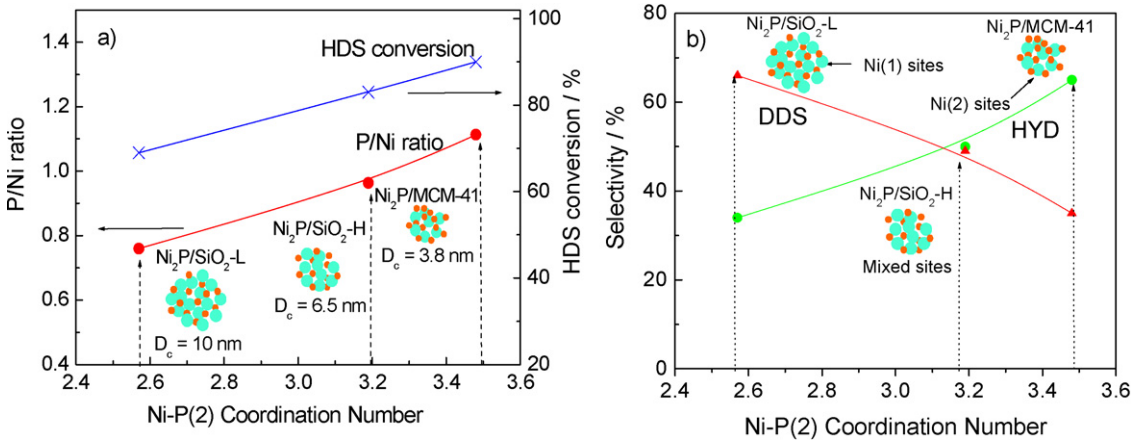

Fig. 7. Correlation of Ni–P(2) coordination numbers with (a) HDS conversion and P/Ni ratio and (b) HYD and DDS selectivity.

4.3. Catalytic behavior of supported Ni_2P catalysts in the HDS of 4,6-DMDBT

The reaction network of 4,6-dimethyldibenzothiophene (4,6-DMDBT) is similar to that of dibenzothiophene, involving two parallel sequences that lead to desulfurized products [53]. One of the parallel pathways is denoted the direct desulfurization pathway (DDS) and in the case of 4,6-DMDBT results in the formation of 3,3′-dimethylbiphenyl (3,3′-DMBP). The other parallel pathway is referred to as the hydrogenation pathway (HYD) and involves the pre-hydrogenation of 4,6-DMDBT to 4,6-tetrahydro- and hexahydro-DMDBT's, which are subsequently desulfurized to methylcyclohexyltoluenes (MCHT) and dimethylbicyclohexane (DMBCH) [54–56]. The two pathways may be distinguished from studies of selectivity extrapolated to low conversions [53]. However, in this work the relative contributions of these pathways were simply approximated by the relative amounts of the final DMBP and DMBCH products. It is realized that these species are interconverted by dehydrogenation/hydrogenation reactions, but it was the main objective of this work to concentrate more on the effect of structure on the HDS rate, than on determining the mechanistic pathways, which had already been addressed [37]. We have examined the role of acidity in previous work, and found that it was associated with phosphorus [57]. The acidity plays a key role in HDN but its effect on HDS is still under examination. The selectivity results (Figs. 4, 5 and 7b) show that as crystallite size decreases the preferred products tend towards hydrogenation products. This indicates that the high activity of the Ni(2) site is associated with superior hydrogenation ability. It may be also deduced that the Ni(1) site is involved in DDS as higher selectivity to the dimethyldiphenyl product is obtained with the catalysts of larger crystallite size. This may be because lower coordination number of the Ni(1) site would allow it to more easily take on a sulfur atom.

It is also noted that the product distribution obtained with the Ni–Mo–S/Al_2O_3 catalysts was similar to that of Ni_2P/MCM-41 (Fig. 5), although the conversion based on equal chemisorptions sites loaded in the reactor was lower. For these catalysts the major products were methylcyclohexyltoluenes (MCHT) and dimethylbicyclohexyl (DMBCH). Only traces of 4,6-tetrahydro- and 4,6-hexahydrodibenzothiophenes were found. It is interesting that in Ni–Mo–S/Al_2O_3 the coordination of the Ni is also square pyramidal [58]. This may again be associated with the high hydrogenation ability of this catalyst.

4.4. Relation to other studies

The effect of structure on catalytic activity may be studied by variation of crystallite size, as carried out in this study, by alloying, or by the use of single crystal models. Previous work in the Ni_2P system will be discussed, and as will be shown the results are consistent with our interpretation that the Ni(2) site is particularly active for hydrogenation and HDS by the HYD route.

A study of silica-supported $Fe_xNi_{2-x}P$ catalysts, which are isostructural with Ni_2P, shows that for $x \sim 0.03$–0.05 the HDS activity is up to 30% higher than that of Ni_2P/SiO_2 [59]. Mössbauer effect measurements in this study confirms results from previous work [60] that for low Fe contents, the Fe occupies the M(1) tetrahedral site, where M is an iron group metal. Since Fe_2P/SiO_2 has considerably lower activity than Ni_2P/SiO_2 [42], two conclusions may be derived. First, the presence of the less active Fe in the M(1) site is not detrimental since it is the M(2) site that is active. Second, the increased activity is likely due to a ligand effect where Fe in the M(1) site affects electronically the Ni in the M(2) site.

Another study of silica-supported $Mo_xNi_{2-x}P$ catalysts, shows that the Mo does not increase the activity of the Ni_2P, but that the activity smoothly decreases as the Mo content increases [28,61], reflecting the higher intrinsic activity of Ni_2P over MoP [21]. For these alloys the Mo is found in the M(2) site [62], so that the activity results are readily interpreted as occurring because of the occupancy of the active M(2) site by the relatively inactive Mo atoms.

Finally, a recent study of Ni_2P single crystals [63] shows that a Ni(0001) face exposing Ni(2) sites is able to activate hydrogen while a face exposing Ni(1) sites is not able to dissociate the hydrogen. This is consistent with the high intrinsic hydrogenation activity of the Ni(2) site observed in the selectivity for HYD products (Table 4, Figs. 4, 5 and 7b).

5. Conclusions

Nickel phosphide (Ni_2P) catalysts supported on silica and MCM-41 showed high HDS activity for 4,6-DMDBT compared to a commercial Ni–Mo–S/Al_2O_3 catalyst at 573 K (300 °C) and 613 K (340 °C) and 3.1 MPa based on equal sites (230 μmol) loaded in the reactor. The crystallite size of the Ni_2P phase decreased from 10.1 to 3.8 nm with increase of the surface area of the support. The desulfurization occurred preferentially by the direct desulfurization (DDS) pathway for the large particle size catalyst but became dominated by the faster hydrogenation (HYD) pathway as the dispersion of the Ni_2P catalysts increased. HYD selectivity and performance was higher on the more dispersed catalysts in the order Ni_2P/MCM-41 > Ni_2P/SiO_2-H > Ni_2P/SiO_2-L and this is attributed to the increase in the number of and quality of active sites. There are two types of sites in Ni_2P, Ni(1) sites with tetrahedral coordination and Ni(2) sites with square pyramidal coordination. EXAFS line shape analysis indicates that both Ni(1) and Ni(2) sites are present on large crystallites but that the Ni(2) sites are more numerous on the more active and more highly dispersed samples. This suggests that in the nickel phosphide phase the lower coordination Ni(1) sites are responsible for desulfurization by the DDS pathway by taking on a sulfur atom while the Ni(2) sites are the high-activity sites that carry out HDS by the HYD route.

Acknowledgments

This work was supported by the US Department of Energy, Office of Basic Energy Sciences, through Grant DE-FG02-963414669 and Brookhaven National Laboratory under Grant 4513 for use of the X18B and X19A beamlines at the National Synchrotron Light Source. We gratefully acknowledge extensive discussions with Profs. Kiyotaka Asakura and Mark Bussell.

References

[1] C. Song, Catal. Today 86 (2003) 211.
[2] P. Greening, Top. Catal. 16/17 (2001) 5.
[3] Y. Yoshimura, M. Toba, H. Farag, K. Sakanishi, Catal. Surv. Asia 8 (2004) 47.
[4] T. Fujikawa, H. Kimura, K. Kiriyama, K. Hagiwara, Catal. Today 111 (2006) 188.
[5] A. Zhou, X. Ma, C. Song, J. Phys. Chem. B 110 (2006) 4699.
[6] J.C. Schlatter, S.T. Oyama, J.E. Metcalfe, J.M. Lambert, Ind. Eng. Chem. Res. 27 (1988) 1648.
[7] H. Abe, T.K. Cheung, A.T. Bell, Catal. Lett. 21 (1993) 11.
[8] S.T. Oyama (Ed.), The Chemistry of Transition Metal Carbides and Nitrides, Blackie Academic and Professional, London, 1996.
[9] W.R.A.M. Robinson, J.N.M. van Gastel, T.I. Korányi, S. Eijsbouts, J.A.R. van Veen, V.H.J. de Beer, J. Catal. 161 (1996) 539.
[10] T.I. Korányi, Appl. Catal. A 239 (2003) 253.
[11] W. Li, B. Dhandapani, S.T. Oyama, Chem. Lett. (1998) 207.
[12] C. Stinner, R. Prins, Th. Weber, J. Catal. 191 (2000) 438.
[13] C. Stinner, R. Prins, Th. Weber, J. Catal. 202 (2001) 187.
[14] P. Clark, W. Li, S.T. Oyama, J. Catal. 200 (2001) 140.
[15] S.T. Oyama, P. Clark, V.L.S. Teixiera da Silva, E.J. Lede, F.G. Requejo, J. Phys. Chem. B 105 (2001) 4961.
[16] C. Stinner, Z. Tang, M. Haouas, Th. Weber, R. Prins, J. Catal. 208 (2002) 456.
[17] S.T. Oyama, P. Clark, X. Wang, T. Shido, Y. Iwasawa, S. Hayashi, J.M. Ramallo-Lopez, F.G. Requejo, J. Phys. Chem. B 106 (2002) 1913.
[18] W. Li, B. Dhandapani, S.T. Oyama, Chem. Lett. (1998) 207.
[19] C. Stinner, R. Prins, T. Weber, J. Catal. 191 (2000) 438.
[20] D.C. Phillips, S.J. Sawhill, R. Self, M.E. Bussell, J. Catal. 207 (2002) 266.
[21] S.T. Oyama, J. Catal. 216 (2003) 343.
[22] N.P. Sweeny, C.S. Rohrer, O.W. Brown, J. Am. Chem. Soc. 80 (1958) 799.
[23] E.L. Muetterties, J.C. Sauer, J. Am. Chem. Soc. 96 (1974) 3410.
[24] F. Nozaki, R. Adachi, J. Catal. 40 (1975) 166.
[25] F. Nozaki, M. Tokumi, J. Catal. 79 (1983) 207.
[26] V. Zuzaniuk, R. Prins, J. Catal. 219 (2003) 85.
[27] Z. Wu, F. Sun, W. Wu, Z. Feng, C. Liang, Z. Wei, C. Li, J. Catal. 222 (2004) 41.
[28] F. Sun, W. Wu, Z. Wu, J. Guo, Z. Wei, Y. Yang, Z. Jiang, F. Tian, C. Li, J. Catal. 228 (2004) 298.
[29] S.J. Sawhill, K.A. Layman, D.R. Van Wyk, M.H. Engelhard, C. Wang, M.E. Bussell, J. Catal. 231 (2005) 300.
[30] Y.-K. Lee, Y. Shu, S.T. Oyama, Appl. Catal. 322 (2007) 191.
[31] Y. Shu, Y.-K. Lee, S.T. Oyama, Chem. Commun. (2005) 1143.
[32] Y. Shu, S.T. Oyama, Carbon 43 (2005) 1517.
[33] P. Liu, J.A. Rodriguez, T. Asakura, J. Gomes, K. Nakamura, J. Phys. Chem. B 109 (2005) 4575.
[34] A.E. Nelson, M. Sun, A.S.M. Junaid, J. Catal. 241 (2006) 180.
[35] P. Clark, S.T. Oyama, J. Catal. 218 (2003) 78.
[36] P. Clark, X. Wang, S.T. Oyama, J. Catal. 207 (2002) 256.
[37] D.C. Phillips, S.J. Sawhill, R. Self, M.E. Bussell, J. Catal. 207 (2002) 266.
[38] S.T. Oyama, X. Wang, Y.-K. Lee Bando, F.G. Requejo, J. Catal. 210 (2002) 207.
[39] T.I. Korányi, Z. Vít, D.G. Poduval, R. Ryoo, H.S. Kim, E.J.M. Hensen, J. Catal. 253 (2008) 119.
[40] J.A. Rodriguez, J.-Y. Kim, J.C. Hanson, S.J. Sawhill, M.E. Bussell, J. Phys. Chem. B 107 (2003) 6276.
[41] J.A. Rodriguez, J. Phys. Chem. B 101 (1997) 7524.
[42] X. Wang, P. Clark, S.T. Oyama, J. Catal. 208 (2002) 321.
[43] S.T. Oyama, X. Wang, Y.-K. Lee, W.-J. Chun, J. Catal. 221 (2004) 263.
[44] C.-F. Cheng, D.H. Park, J. Klinowski, J. Chem. Soc. Faraday Trans. 93 (1) (1997) 193.
[45] B.D. Cullity, Elements of X-Ray Diffraction, second ed., Addison–Wesley, Menlo Park, CA, 1978, p. 102.
[46] P.T. Tanev, L.T. Vlaev, J. Colloid Interface Sci. 160 (1993) 110.
[47] A.L. Ankudinov, B. Ravel, J.J. Rehr, S.D. Congradson, Phys. Rev. B 58 (1998) 7565.
[48] S. Rundqvist, Acta Chem. Scand. 16 (1962) 992.
[49] A. Infantes-Molina, J. Mérida-Robles, P. Braos-García, E. Rodríguez-Castellón, E. Finocchio, G. Busca, P. Maireles-Torres, A. Jiménez-López, J. Catal. 225 (2004) 479.
[50] A.L. Ankudinov, B. Ravel, J.J. Rehr, S.D. Congradson, Phys. Rev. B 58 (1998) 7565.
[51] E.A. Stern, Phys. Rev. B 48 (1993) 9825.
[52] Y. Shu, Y.-K. Lee, S.T. Oyama, J. Catal. 236 (2005) 112.
[53] J.H. Kim, C. Song, Y.-K. Lee, S.T. Oyama, Energy Fuels 19 (2005) 353.
[54] D.D. Whitehurst, T. Isoda, I. Mochida, Adv. Catal. 42 (1998) 345.
[55] K. Segawa, S. Satoh, Stud. Surf. Sci. Catal. 127 (1999) 129.
[56] M. Egorova, R. Prins, J. Catal. 224 (2004) 278.
[57] Y.-K. Lee, S.T. Oyama, J. Catal. 239 (2006) 376.
[58] M. Egorova, R. Prins, J. Catal. 241 (2006) 162.
[59] A.W. Burns, A. Gaudette, T. Seda, M.E. Bussell, private communication.
[60] Y. Maeda, Y. Takashima, J. Inorg. Nucl. Chem. 35 (1973) 1963.
[61] J.A. Rodriguez, J.-Y. Kim, J.C. Hanson, S.J. Sawhill, M.E. Bussell, J. Phys. Chem. B (2003) 6276.
[62] P.R. Guérin, M. Sergent, Acta Cryst. B 33 (1977) 2820–2823.
[63] S. Suzuki, G. Md. Moula, Y. Nakagawa, K. Kinoshita, T. Miyamoto, K. Asakura, S.T. Oyama, S. Ohtani, J. Nanosci. Nanotech. (2008), in press.